

Ultraviolet Probing of Quantum Crossbars

I. Kuzmenko¹, S. Gredeskul¹, K. Kikoin¹, and Y. Avishai^{1,2}

¹*Department of Physics and* ²*Ilse Katz Center, Ben-Gurion University, Beer-Sheva, Israel*

(Dated: November 13, 2018)

Ultraviolet (UV) scattering on quantum crossbars (QCB) is an effective tool for probing QCB spectral properties, leading to excitation of QCB plasmon(s). Experimentally, such a process corresponds to sharp peaks in the frequency dependence of the differential scattering cross section. The peak frequency strongly depends on the direction of the scattered light. As a result, $1D \rightarrow 2D$ crossover can be observed in the scattering spectrum. It manifests itself as a splitting of single lines into multiplets (mostly doublets). The splitting magnitude increases with interaction in QCB crosses, while the peak amplitudes decrease with electron-electron interaction within a QCB constituent.

PACS numbers: 78.67.-n, 78.30.-j, 73.90.+f

I. INTRODUCTION

Quantum crossbars (QCB) is a novel artificial nano-object which represents actually a double $2D$ grid formed by two superimposed crossing arrays of parallel conducting quantum wires^{1,2,3,4}, molecular chains⁵ or metallic single wall carbon nanotubes (SWCNT)^{4,6,7,8}. Similar structures with the same crossbar geometry also arise naturally as, e.g., crossed striped phases of doped transition metal oxides⁹. The QCB mechanical flexibility together with the possibility of exciting some of its constituents (nanotube, a single wire) by external electric field and the existence of bistable conformations of others (molecular chain¹⁰) makes QCB one of the most attractive architectures for designing molecular-electronic circuits for computational application^{5,6,11}. One more attractive property of QCB, its optical activity in a wide frequency region from infrared (IR) to ultraviolet (UV) one, will be discussed in the present paper.

From a geometrical point of view, QCB is, in a sense, an object with intermediate dimensionality. The two dimensional character of QCB as a whole, together with the one dimensional character of its constituents enables studying the crossover from a $1D$ Luttinger liquid (LL) behavior to a $2D$ Fermi liquid (FL) behavior. Indeed, a single wire or nanotube possesses the LL-like spectrum^{12,13}. An array of parallel wires is still a LL-like system (qualified as a sliding phase⁷) provided the pure electrostatic interaction between adjacent wires is taken into account. However, inter-wire tunneling turns the electronic spectrum of an array to that of $2D$ FL^{14,15}. A system of two crossing arrays (QCB) manifests the same behavior. Being coupled only by capacitive interaction in the crosses, they have similar low-energy, long-wave properties characterized as a crossed sliding LL phase^{7,16}. Inter-array electron tunneling destroys the LL behavior at low energies and results in dimensional crossover to $2D$ FL^{7,17,18}. Here the control parameter which rules the crossover is the tunneling intensity.

Outside the low energy region, the intermediate character of the QCB dimensionality leads to nontrivial spectral properties which cannot be treated in terms of

purely $1D$ or purely $2D$ electron liquid theory. QCB with only electrostatic interaction in the crosses possesses the LL zero energy fixed point. Far from this point, the system conserves a Bose character in the absence of interwire tunneling but the dimensionality of its Bose excitations (plasmon modes) becomes intermediate between $1D$ and $2D$ in spite of the fact that they live in the $2D$ Brillouin zone (BZ)^{16,19}. These QCB plasmons can be treated as a set of dipoles within the QCB constituents. In a single wire, the density of their dipole momenta is proportional to the LL boson field $\theta(x)$ (x is the coordinate along the wire). In QCB, there are two sets of coupled dipoles. They form a unique system which manifests either $1D$ or $2D$ properties depending on details of the relevant experiment. This results in a new dimensional crossover. It differs from the LL to FL transition mentioned above and is ruled by other control parameters (quasimomentum, energy, frequency of an external field and so on). Some possibilities of observing such crossover in transport measurements (which give information about the nearest vicinity of the LL fixed point at $(q, \omega, T) \rightarrow 0$) were discussed in Ref.7. Other crossover effects such as appearance of non-zero transverse space correlation functions and periodic energy transfer between arrays ("Rabi oscillations") were studied in Ref.19. Observation of these effects probes the QCB spectral properties outside the LL fixed point (i.e. well beyond the crossing sliding phase region).

A rather pronounced manifestation of these kinds of dimensional crossover is related to QCB response to an external ac electromagnetic field. The two main parameters characterizing the plasmon spectrum in QCB are the velocity v of plasmons in a single wire and the QCB period a (we assume that periods in the two basic directions are equal). These parameters define both the typical plasmon wave numbers $Q_0 = 2\pi/a$ and their typical frequencies $\omega_0 = vQ_0$. Choosing $v \approx 8 \cdot 10^7$ cm/sec and $a \approx 20$ nm, according to Refs.[6,13], one finds that plasmon frequencies lie in the far infrared (IR) region $\omega \sim 10^{14}$ sec⁻¹, while characteristic order of plasmon wave vectors is $Q_0 \sim 10^6$ cm⁻¹.

A very natural method to study the QCB spectrum

is by means of optical spectroscopy. The characteristic values of QCB frequencies and wave vectors determine two possible directions of such an experimental observation. The first one is IR spectroscopy of QCB where *the frequency* of an external ac field lies at the same region as the QCB frequency. The second one is an UV scattering on QCB where *the wave vector* of a scattered field lies in the same region as that of the QCB wave vectors.

The effectiveness of IR spectroscopy of QCB were studied in Refs. 20,21. Here, the IR light wave vector k is three orders of magnitude smaller than the characteristic plasmon wave vector Q_0 (the plasmon velocity v is much smaller than the light velocity c). Therefore, an infrared radiation incident on an *isolated* array, can excite plasmon only with $\omega = 0$, or simply speaking, cannot excite plasmons at all. However in the QCB geometry, each array serves as a diffraction lattice for its partner, giving rise to Umklapp processes with Umklapp vectors say $(nQ_0, 0)$ with an integer n . As a result, excitation of plasmons in the BZ center with frequencies $\omega = nvQ_0$ is possible.

To excite QCB plasmons with non zero wave vectors, an additional diffraction lattice with period $A > a$ coplanar with the QCB can be used. Here the diffraction field contains space harmonics with wave vectors $2\pi M/A$ (M integer), that enables one to eliminate the wave vector mismatch and to scan plasmon spectrum within the BZ. In the general case, one can observe single absorption lines forming two equidistant sequences. However, in case where the wave vector of the diffraction field is oriented along some resonance directions, additional absorption lines appear. As a result, an equidistant sequences of split doublets can be observed in the main resonance direction (BZ diagonal). This is the central concept of dimensional crossover mentioned above with direction serving as a control parameter. In higher resonance directions, absorption lines form an alternating series of singlets and split doublets demonstrating new type of dimensional crossover. The latter occurs in a given direction with frequency as a control parameter.

One more version of IR QCB spectroscopy is related to the study of QCB placed onto a semiconductor substrate^{20,21}. It occurs that a capacitive contact between the QCB and the substrate does not destroy the LL character of the long wave QCB excitations. However, the dielectric losses of a substrate are drastically modified due to diffraction processes on the QCB superlattice. QCB - substrate interaction results in the appearance of additional Landau damping regions of the substrate plasmons. Their existence, form, and density of losses are strongly sensitive to variation of the QCB lattice constant.

The IR based methods mentioned above are not very convenient from two points of view. First, as it was mentioned, one needs an additional diffraction lattice

to tune the light wave vector and that of the QCB plasmon. Second, they probe QCB spectrum only in some discrete points. The alternative method of studying QCB spectrum by *ultraviolet (UV) light scattering* is the subject of the present paper. The advantages of this method are evident. It does not require any additional diffraction lattice. It probes QCB spectrum in a continuous region of wave vectors. Finally, its selection rules differ from those for IR absorption. This gives rise to the observation of additional spectral lines not visible in IR experiments.

In this paper we formulate the principles of UV spectroscopy for QCB and study the main characteristics of scattering spectra. The paper is organized as follows. In subsection II A, we briefly describe double square QCB and quantum numbers associated with its excitations. In the next subsection, II B, we discuss light scattering on QCB and present basic equations describing this process. The main results of the paper are contained in Section III where we classify the basic types of the scattering indicatrices (angular diagrams of differential cross section) corresponding to various detector orientations. The results obtained are summarized in the Conclusions. Technical details are concentrated in two Appendices. Representation of QCB plasmons in terms of array plasmons is explained in Appendix A. Appendix B is devoted to the derivation of an effective QCB-light interaction. The basic formulas for differential cross section of light scattering are concentrated in this Appendix.

II. LIGHT SCATTERING ON QCB

A. QCB: Geometry, Hamiltonian, Spectrum

A square QCB is formed by two periodically crossed perpendicular arrays of 1D quantum wires or carbon nanotubes. The two arrays are lying on two parallel planes separated by an inter-plane distance d (see Fig. 1). They are labeled by indices $j = 1, 2$ and wires within the first (second) array are labeled by an integer index n_2 (n_1). The coordinate system in Fig. 1 is chosen such that (i) the axes x_j and the corresponding basic unit vectors \mathbf{e}_j are oriented along the j -th array; (ii) the x_3 axis is perpendicular to the QCB plane; (iii) the x_3 coordinate is zero for the first array and d for the second one. A single wire is characterized by its radius r_0 , length L , and LL interaction parameter g . The minimal nanotube radius is $r_0 \approx 0.35$ nm²², maximal nanotube length is $L \approx 1$ mm, and the LL parameter is estimated as $g \approx 0.3$ ¹³. Typical QCB period and inter-array distance are $a \approx 20$ nm, $d \approx 2$ nm⁶ so that usually $r_0 \ll d \ll a \ll L$.

The QCB Hamiltonian is

$$H_{QCB} = H_1 + H_2 + H_{12}. \quad (1)$$

The first term H_1 describes LL in the first array

$$H_1 = \frac{\hbar v}{2} \sum_{n_2} \int_{-L/2}^{L/2} dx_1 \left\{ g\pi_1^2(x_1, n_2 a, 0) + \frac{1}{g} (\partial_{x_1} \theta_1(x_1, n_2 a, 0))^2 \right\}, \quad (2)$$

where $\theta_1(x, y, z)$ and $\pi_1(x, y, z)$ are two the conventional canonically conjugate boson fields of the first array. Its counterpart H_2 describes the second array and is obtained from H_1 by permutation $1 \leftrightarrow 2$ and a replacement $0 \rightarrow d$ in the arguments of the fields.

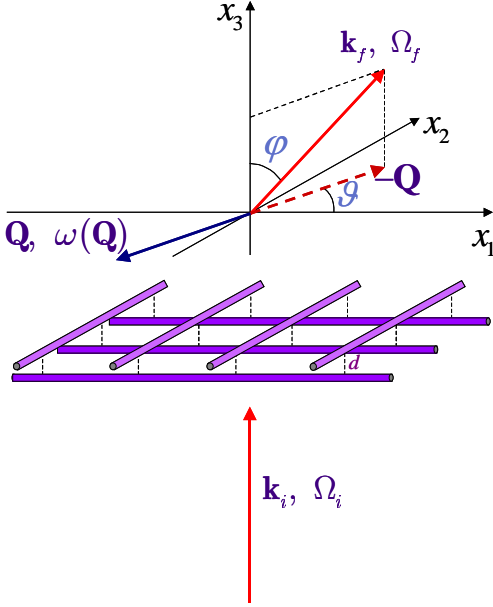


FIG. 1: The scattering process geometry (all notations are explained in the text).

The third term in Eq.(1) H_{12} describes the capacitive inter-array interaction. It has a separable form

$$H_{12} = V_0 \sum_{n_1, n_2} \int_{-L/2}^{L/2} dx_1 dx_2 \times \zeta \left(\frac{x_1 - n_1 a}{r_0} \right) \zeta \left(\frac{n_2 a - x_2}{r_0} \right) \times \partial_{x_1} \theta_1(x_1, n_2 a, -d) \partial_{x_2} \theta_2(n_1 a, x_2, 0), \quad (3)$$

$$V_0 = \frac{2e^2}{d}.$$

and is localized around the QCB crosses¹⁹. This form of inter-array interaction is actually a limiting form of an exact inter-array Coulomb interaction for $r_0/d \ll 1$ taking into account electron screening in a single nanotube²³.

The Hamiltonian (1), (2), (3) describes QCB in the absence of tunneling. In real QCB with typical parameters mentioned above, an interwire tunneling is rather

small⁶. Coulomb blockade accompanying charging of adjacent tubes in a process of electron transition from one tube to another, suppresses these processes. Only electron-hole cotunneling without recharging is possible, and this cotunneling slightly renormalizes the coefficient V_0 in Eq. (3). The corresponding relative correction is of order of 10^{-4} .

The coordinates d and 0 along the third spatial direction x_3 enter the QCB dynamics as parameters. It is natural to expect that QCB possesses of $2D$ spectral properties which can be classified by $2D$ quasi-momentum. The basic vectors of the $2D$ reciprocal superlattice are $Q_0 \mathbf{e}_j$, $j = 1, 2$, so that any vector of the reciprocal superlattice \mathbf{m} is a sum $\mathbf{m} = \mathbf{m}_1 + \mathbf{m}_2$, where $\mathbf{m}_j = m_j Q_0 \mathbf{e}_j$ with integer m_j . The first BZ of QCB is $|Q_j| < Q_0/2$ (see Fig. 2). An arbitrary vector $\mathbf{Q} = (Q_1, Q_2)$ of reciprocal space can be written as $\mathbf{Q} = \mathbf{q} + \mathbf{m}$, where $\mathbf{q} = (q_1, q_2)$ belongs to the first BZ. QCB eigenstates are classified by quasi-momentum \mathbf{q} and $2D$ band number S .

However, the specific QCB geometry makes its spectral properties rather unusual. Consider an *isolated* array 1. Within the (x_1, x_2) plane, its excitations are described by a pair of $2D$ coordinates $(x_1, n_2 a)$, i.e. a continuous longitudinal coordinate x_1 parallel to the \mathbf{e}_1 direction, and its discrete transverse partner $n_2 a$ parallel to \mathbf{e}_2 . As a result, the longitudinal component $Q_1 = q_1 + m_1 Q_0$ of the excitation momentum changes on the entire axis $-\infty < Q_1 < \infty$ while its transverse momentum q_2 is restricted to the region $|q_2| < Q_0/2$. Thus an eigenstate (plasmon) of the first array is characterized by the vector $\mathbf{Q}_1 = \mathbf{q} + \mathbf{m}_1 = (Q_1, q_2)$ and the frequency

$$\omega_1(\mathbf{Q}_1) = v|Q_1|$$

which depends only on the longitudinal component Q_1 of the momentum \mathbf{Q}_1 . Similar description for the second array is obtained by replacing $1 \leftrightarrow 2$.

In the case of "empty lattice" (QCB with infinitesimal interaction between arrays, $V_0 \rightarrow 0$) the complementary second array produces infinitely small periodic potential which affects the first array. The vector \mathbf{m}_1 becomes a reciprocal $1D$ lattice vector and \mathbf{q} becomes the $2D$ quasi-momentum. The first array excitations are labeled by this $2D$ quasi-momentum \mathbf{q} and $1D$ band number

$$s_1 = \left[\frac{2|Q_1|}{Q_0} \right] + 1$$

(square brackets denote an integer part of the number). The corresponding dispersion law has the form

$$\omega_{s_1}(\mathbf{q}) \equiv \omega_1(\mathbf{Q}_1) = v|Q_1| = vQ_0 \left(\left[\frac{s_1}{2} \right] + (-1)^{s_1-1} \frac{|q_1|}{Q_0} \right).$$

As in the previous paragraph, by replacing $1 \leftrightarrow 2$, we obtain formulas describing eigenstates of the second array

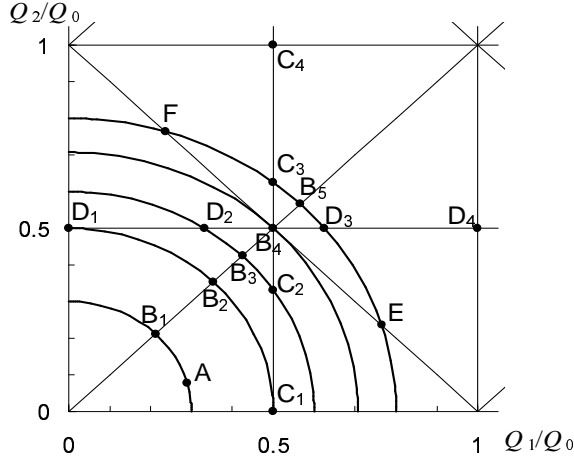


FIG. 2: Part of the reciprocal space. The small square $Q_j/Q_0 \leq 0.5$ is the quarter of the first QCB BZ. High symmetry lines are parallel to the coordinate axes. Resonant lines are parallel to BZ diagonals. The arcs coming over the point B_1, B_2, B_3, B_4, B_5 , correspond to different wave numbers of the excited plasmons: $|Q/Q_0| = 0.3; 0.5; 0.6; 0.7; 0.8$.

embedded into an "empty lattice". Thus an arbitrary vector $\mathbf{Q} = \mathbf{q} + \mathbf{m}_1 + \mathbf{m}_2 = (Q_1, Q_2)$ of the reciprocal space generates two vectors $\mathbf{Q}_1 = \mathbf{q} + \mathbf{m}_1 = (q_1, q_2)$ and $\mathbf{Q}_2 = \mathbf{q} + \mathbf{m}_2 = (q_1, q_2)$. The "empty QCB" eigenstates are labelled by one of these vectors and its array number. Each one of the eigenstates propagates along the corresponding array.

The dimensionless strength of the inter-array interaction (3) of QCB with typical values of the parameters is small,

$$\phi = \frac{gV_0 r_0^2}{\hbar v a} \approx 0.007. \quad (4)$$

As a result, QCB eigenstates approximately conserve the same quantum numbers as the (unperturbed) eigenstates of an "empty QCB". These numbers are array numbers $j = 1, 2$, and the corresponding vectors \mathbf{Q}_j . In the general case, there are two QCB eigenstates associated with each wave vector \mathbf{Q} of reciprocal space. In zeroth approximation, these QCB eigenstates coincide with the "empty QCB" eigenstates

$$\begin{aligned} |1, \mathbf{Q}_1\rangle &= a_{1, \mathbf{Q}_1}^\dagger |0\rangle, \\ |2, \mathbf{Q}_2\rangle &= a_{2, \mathbf{Q}_2}^\dagger |0\rangle, \end{aligned} \quad (5)$$

where a^\dagger is an array of plasmon creation operators and $|0\rangle$ is the bosonic vacuum. The corresponding eigenfrequencies coincide with the unperturbed frequencies

$$\omega_j(\mathbf{Q}_j) = v|Q_j|, \quad j = 1, 2, \quad (6)$$

in the same approximation. In higher orders of perturbation, the r.h.s. of Eq. (5) includes additional terms like $a_{1, \mathbf{Q}_1 + \mathbf{m}}^\dagger |0\rangle$, where \mathbf{m} is an arbitrary reciprocal lattice vector. However, the coefficients before these terms are

of higher order of magnitude with respect to the small inter-array interaction (4).

Such a simple description fails at the points \mathbf{Q} lying on two specific groups of lines in reciprocal space (see Appendix A for details). Nevertheless, even at these points QCB plasmons are represented as a finite superposition of array plasmons with coefficients of order unity. As the point \mathbf{Q} moves away from a specific line, only one of these coefficients survives while all other decrease rapidly. So more complicated structure of QCB plasmons at the specific lines, presented in Appendix A, turns to the standard description (5) within narrow transition strips which adjoin to the specific lines. Out of these strips, i.e. in major part of reciprocal space (including the nearest vicinities of the specific lines), a point \mathbf{Q} completely determines the structure of all possible QCB plasmons with momentum \mathbf{Q} .

B. Light scattering

The simplest process contributing to Raman-like light scattering is an annihilation of an incident photon and creation of a scattered photon together with a QCB plasmon (Fig. 3a). In terms of initial electrons, this is in fact a second order process. Since the energies of incident and scattered photons significantly exceed the electron excitation energy in the nanotube, one may consider the emission/absorption process as an instantaneous act (see Appendix B). This process may be treated as an inelastic photon scattering accompanied by emission or absorption of a plasmon (Fig. 3b).

Let \mathbf{k}_i (\mathbf{k}_f) and $\Omega_i = ck_i \equiv c|\mathbf{k}_i|$, ($\Omega_f = ck_f$) be momentum and frequency of the incident (scattered) photon. For simplicity we restrict ourselves by the case of normal incidence $\mathbf{k}_i = (0, 0, k_i)$. Direction of the scattered wave vector is characterized by a unit vector $\mathbf{n}(\varphi, \vartheta)$, where φ and ϑ are polar and azimuthal angles in the spherical coordinate system with polar axis directed along \mathbf{e}_3 direction. The momentum of the excited QCB plasmon is $\mathbf{Q} = -\mathbf{K}$, where \mathbf{K} is the projection of the scattered photon momentum \mathbf{k}_f onto the QCB plane. This process is displayed in Fig. 1. If the QCB plasmon frequency $\omega(\mathbf{Q})$ coincides with the photon frequency loss $\omega = \Omega_i - \Omega_f$, then a detector oriented in a scattered direction \mathbf{n} will register a sharp well pronounced peak at the frequency loss $\omega = \omega(\mathbf{Q})$. The frequency loss is much smaller than the incident and scattered photon frequencies. Therefore in what follows we use the same notation k for both k_i and k_f where it is possible. Scanning the frequency loss ω , (or, equivalently, the modulus of the scattered wave vector

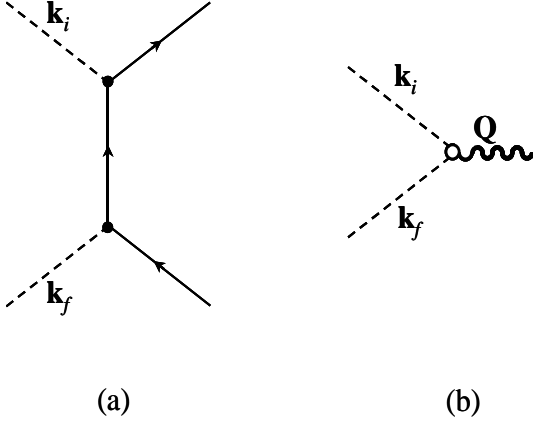


FIG. 3: (a) Second order diagram describing light scattering on QCB. Solid lines correspond to fermions, whereas dashed lines are related to photons. The vertices are described by the interaction Hamiltonian (7). (b) Effective photon-plasmon interaction. QCB excitation is denoted by wavy line.

k_f) for a fixed detector orientation \mathbf{n} , two or more (up to six for a square QCB) such peaks can be observed. The number of peaks and their location depend strongly on the azimuthal angle ϑ in the QCB plane. Scanning this angle, one can change the number of observable peaks. This is yet another manifestation of dimensional crossover mentioned above.

The scattering differential cross section is smooth function of ω . However, in zeroth approximation, only the peaks survive (smooth background is very low because of weak inter-array interaction). Therefore in a chosen approximation, the scattering cross section is characterised by a number of peaks, their positions and intensities. Calculation of these quantities as functions of the frequency loss ω and azimuthal angle ϑ for various fixed values of the polar angle φ , is the main goal of our study.

To perform quantitative analysis, we should derive an expression for the scattering cross section. Details of all calculations are given in Appendix B. Here we present only the main steps of the derivation. We start from the Hamiltonian

$$h_{nl} = \frac{ev_F}{c} \int \frac{dx_1 d\gamma}{2\pi} \psi_\alpha^\dagger \mathbf{A} \cdot \boldsymbol{\sigma}_{\alpha,\alpha'} \psi_{\alpha'}, \quad (7)$$

which describes interaction between a single nanotube oriented e.g. along \mathbf{e}_1 (the first array nanotube) and an external electromagnetic field. The field is described by its vector potential in the Landau gauge

$$\mathbf{A} = A_1 \mathbf{e}_1 + A_2 \mathbf{e}_2 + A_3 \mathbf{e}_3. \quad (8)$$

The indices $\alpha = a, b$ enumerate sublattices in a honeycomb carbon sheet, (r, γ) are polar coordinates in the (x_2, x_3) plane, $\psi_\alpha(x_1, \gamma) \equiv \psi_\alpha(x_1, r_0, \gamma)$ and ψ_α^\dagger are slowly varying electron field operators at the nanotube

surface $r = r_0$, and the vector of Pauli matrices $\boldsymbol{\sigma}$ is

$$\begin{aligned} \boldsymbol{\sigma} &= \mathbf{e}_1 \sigma_x + \mathbf{e}_\gamma \sigma_y \\ \mathbf{e}_\gamma &= -\mathbf{e}_2 \sin \gamma + \mathbf{e}_3 \cos \gamma. \end{aligned}$$

The light wavelength is much larger than the nanotube radius, so the vector potential can be taken at its axis, $\mathbf{A}(x_1, 0, 0)$.

Such form of a nanotube-light interaction leads to the following expression for an effective QCB-light interaction Hamiltonian

$$\begin{aligned} H_{int} &= \frac{\sqrt{2}}{4k} \frac{e^2}{\hbar c} \left(\frac{v_F}{c} \right)^2 \sum_{n_2} \int dx_1 \times \\ &\quad \times \partial_{x_1} \theta_1(x_1, n_2 a) \mathbf{A}_1^2(x_1, n_2 a, 0) + \\ &+ \frac{\sqrt{2}}{4k} \frac{e^2}{\hbar c} \left(\frac{v_F}{c} \right)^2 \sum_{n_1} \int dx_2 \times \\ &\quad \times \partial_{x_2} \theta_2(n_1 a, x_2) \mathbf{A}_2^2(n_1 a, x_2, d). \end{aligned} \quad (9)$$

Here

$$\mathbf{A}_j(\mathbf{r}) = \mathbf{A}(\mathbf{r}) + (\sqrt{2} - 1) A_j(\mathbf{r}) \mathbf{e}_j, \quad j = 1, 2,$$

are two effective vector potentials affecting the two arrays and $A_j(\mathbf{r})$ are two (out of three) cartesian components of the full vector potential (8). The main object of our interest is the scaled differential cross-section $\sigma(\omega, \mathbf{n})$ of the scattering defined by

$$d\sigma = L^2 \frac{g}{4\pi k a} \left(\frac{e^2}{\hbar c} \right)^2 \left(\frac{v_F}{c} \right)^4 \sigma(\omega, \mathbf{n}) d\omega d\varphi d\vartheta, \quad (10)$$

where L^2 is the QCB area and $d\varphi = \sin \varphi d\varphi d\vartheta$. A standard procedure applied to the Hamiltonian (9), leads to the following form of the scaled cross section

$$\sigma(\omega, \mathbf{n}) = \frac{1}{4k} \sum_P \overline{|\langle P | h | 0 \rangle_P|^2} \delta(\omega - \omega_P). \quad (11)$$

Here $\omega = \Omega_i - \Omega_f$ is the frequency loss and

$$\begin{aligned} h &= - \sum_j \frac{K_j}{\sqrt{|K_j|}} \times \\ &P_{j;\lambda_f, \lambda_i}(\varphi, \vartheta) \left(a_{j, \mathbf{K}_j} + a_{j, -\mathbf{K}_j}^\dagger \right) \end{aligned} \quad (12)$$

is the interaction Hamiltonian reduced to the subspace of QCB states. Summation is performed over all one-plasmon states $|P\rangle$. The vector \mathbf{K}_j is obtained from \mathbf{K}_f in the same way as the vector \mathbf{Q}_j is obtained from \mathbf{Q} , and $P_{j;\lambda_f, \lambda_i}(\varphi, \vartheta)$, $j = 1, 2$, are polarization matrices. In the basis (\parallel, \perp) they are

$$\begin{aligned} P_1(\varphi, \vartheta) &= - \begin{pmatrix} 2 \sin \vartheta & i \cos \vartheta \\ 2i \cos \vartheta \cos \varphi & \sin \vartheta \cos \varphi \end{pmatrix}, \\ P_2(\varphi, \vartheta) &= P_1\left(\frac{\pi}{2} + \vartheta, \varphi\right). \end{aligned} \quad (13)$$

Equations (11) - (13) serve as a basis for the subsequent analysis.

III. SCATTERING CROSS SECTION

A. Cross section: Basic types

According to Eqs. (11), (12), in order to contribute to the cross-section (11) in a fixed detector orientation at \mathbf{n} , an excited QCB plasmon $|P\rangle$ must contain at least one of two single-array states $|1, -\mathbf{K}_1\rangle$ or $|2, -\mathbf{K}_2\rangle$. Analysis shows that there are five basic types of excited QCB plasmons depending on the location of the point \mathbf{Q} . Here we describe these types of plasmons and the corresponding structure of the differential cross section of scattering. In this description, beside the polar angle φ of the scattered photon wave vector \mathbf{k}_f , we use, in a sense, a mixed representation. It is based on the excited plasmon momentum $\mathbf{Q} = -\mathbf{K}$ and the azimuthal angle ϑ of the transverse component of the scattered photon wave vector \mathbf{K} .

i. General case: The point \mathbf{Q} lies away from both the high symmetry lines and the resonant lines. This case is illustrated by the point A in Fig. 2. There are two QCB plasmons $|P\rangle$, Eqs. (5), with frequencies (6), which contribute to the scattering. The differential cross-section is a sum of two peaks centered at these frequencies. After averaging over initial and final polarizations, it has the form

$$\sigma(\omega, \mathbf{n}) = F_1(\mathbf{n})\delta(\omega - \omega_1) + F_2(\mathbf{n})\delta(\omega - \omega_2),$$

where the functions

$$\begin{aligned} F_1(\mathbf{n}) &= F(\varphi, \vartheta) = |\sin \varphi \cos \vartheta| \times \\ &\quad \left[1 - \frac{3}{4} \sin^2 \varphi \cos^2 \vartheta + \frac{1}{4} \cos^2 \varphi \right], \\ F_2(\mathbf{n}) &= F\left(\varphi, \vartheta + \frac{\pi}{2}\right), \end{aligned}$$

describe universal angle dependences of the peak amplitudes. The functions $F_{1,2}$ are related to the corresponding array plasmons. Each one of them vanishes when the scattered photon is perpendicular to the corresponding array. However these functions describe the scaled cross section. The absolute value amplitude of each peak has an additional factor $\frac{g}{4\pi k a} \left(\frac{e^2}{\hbar c}\right)^2 \left(\frac{v_F}{c}\right)^4$. Strong electron-electron interaction in a nanotube corresponds to small values of the Luttinger parameter g and therefore suppresses the scattering cross section.

ii. Inter-band resonance in one of the arrays: the point \mathbf{Q} lies on a high symmetry line of only one array. This case is illustrated by the points $C_{2,3}$ (1-st array) and $D_{2,3}$ (2-d array) in Fig. 2. Consider for example point C_2 where $Q_1 = Q_0/2$, $Q_2 \neq nQ_0/2$. Here *three* QCB plasmons contribute to the scattering. The first is a $|2, Q_2\rangle$ plasmon, (5), with frequency ω_2 , Eq. (6). The other two are even or odd superpositions of the 1-st array states (Eq. (A1) with $j = 1$) of the two first zones with eigenfrequencies (A2). Due to weakness of the inter-array interaction, three peaks of the scattering cross

section form a singlet ω_2 and doublet ω_{1g}, ω_{1u} . After averaging over initial and final polarizations, the cross section has the form

$$\begin{aligned} \sigma(\omega, \mathbf{n}) &= \frac{1}{2} F_1(\mathbf{n}) [\delta(\omega - \omega_{1g}) + \delta(\omega - \omega_{1u})] \\ &+ F_2(\mathbf{n}) \delta(\omega - \omega_2). \end{aligned}$$

iii. Inter-band resonance in both arrays: The point \mathbf{Q} is a crossing point of two high symmetry lines away from all resonant lines. This case is illustrated by the points C_4 and D_4 in Fig. 2. Consider for example point C_4 . Here $Q_1 = Q_0/2$, $Q_2 = 2Q_0/2$, and *four* QCB plasmons contribute to the scattering. The first pair consists of even and odd superpositions of the 1-st array states of the first and the second bands. These states and their frequencies are described by Eqs. (A5), (A6) with $j = 1$. The second pair consists of the same superpositions of the 2-d array states from the second and third bands and is described by the same equations with $j = 2$. As a result, *four* peaks, which form two doublets (A6), $j = 1, 2$, can be observed. After averaging over initial and final polarizations the cross section is

$$\begin{aligned} \sigma(\omega, \mathbf{n}) &= \frac{1}{2} F_1(\mathbf{n}) [\delta(\omega - \omega_{1g}) + \delta(\omega - \omega_{1u})] \\ &+ \frac{1}{2} F_2(\mathbf{n}) [\delta(\omega - \omega_{2g}) + \delta(\omega - \omega_{2u})]. \end{aligned}$$

iv. Inter-array resonance: The point \mathbf{Q} lies only on one of the resonant lines away from the high symmetry lines. This case is illustrated by the points $B_{1-3,5}$, E , and F in Fig. 2. Here the QCB plasmons which contribute to the scattering are two even and two odd superpositions of the first and second array states (A3) whose eigenfrequencies form two doublets (A4). As in the previous case, the scattering cross section contains *four* peaks which form two doublets. After averaging over initial and final polarizations the cross section is

$$\begin{aligned} \sigma(\omega, \mathbf{n}) &= \frac{1}{2} F_1(\mathbf{n}) [\delta(\omega - \omega_g(\mathbf{Q}_1)) + \delta(\omega - \omega_u(\mathbf{Q}_1))] + \\ &\frac{1}{2} F_2(\mathbf{n}) [\delta(\omega - \omega_g(\mathbf{Q}_2)) + \delta(\omega - \omega_u(\mathbf{Q}_2))]. \end{aligned}$$

Thus, the inter-array splitting is proportional to the central small parameter of the theory, ϕ (see Eq. (4)). For the set of parameters described in the beginning of subsection II A, the interband splitting defined by Eq. (A2), is five times smaller because it contains an additional factor $\phi a/r_0$.

v. Inter-array and inter-band resonance: The point \mathbf{Q} lies at the intersection of two resonant lines. There is only one such point B_4 in Fig. 2. In the general case, where the parameter $n \neq 0$ for both crossing resonant lines (the point B_4 is *not* the case), the

QCB plasmons involved in Raman scattering form two quartets. The first quartet consists of four symmetrized combinations (A7) of the single-array states. QCB eigenstates for the second quartet are obtained from these equations by replacing $1 \leftrightarrow 2$. The corresponding eigenfrequencies are described by Eqs. (A8), (A9). The scattering cross section in this case contains six peaks, and two of them are two-fold degenerate

$$\begin{aligned} \sigma(\omega, \mathbf{n}) = & \frac{1}{4} F_1(\mathbf{n}) [2\delta(\omega - \omega_{g,u/g}(\mathbf{Q}_1)) + \\ & \delta(\omega - \omega_{uu}(\mathbf{Q}_1)) + \delta(\omega - \omega_{ug}(\mathbf{Q}_1))] + \\ & \frac{1}{4} F_2(\mathbf{n}) [2\delta(\omega - \omega_{g,u/g}(\mathbf{Q}_2)) + \\ & \delta(\omega - \omega_{uu}(\mathbf{Q}_2)) + \delta(\omega - \omega_{ug}(\mathbf{Q}_2))]. \end{aligned}$$

The point B_4 in Fig. 2 lies on the main resonance line with $n = 0$. Here $|Q_1| = |Q_2|$, the frequencies of both quartets coincide, and the scattering cross section contains one four-fold degenerate peak and a symmetric pair of its two-fold degenerate satellites.

This classification of all types of excited plasmons enables us to describe completely the UV scattering on QCB.

B. Scattering indicatrices

In this subsection we describe the results of the scattering process with the help of a family of scattering indicatrices.

To explain the indicatrix structure, we start with some preliminary arguments. Consider the case where the detector is tuned to the frequency Ω_f and is oriented in the direction \mathbf{n} . These parameters uniquely determine a point $\mathbf{K} = -\mathbf{Q}$. There are two ways of scanning QCB plasmons. The first way is to scan through the polar angle ϑ . The corresponding points \mathbf{K} in Fig. 2 form an arc with radius $K = (\Omega_f/c) \sin \varphi$. The second way is to tune the detector frequency Ω_f . We are interested in frequency loss of order of the plasmon frequencies within the two - three lowest bands. This loss is of order of $\Omega_f(v/c) \ll \Omega_f$. Therefore in this case the point \mathbf{K} remains in its place (with a very good accuracy).

Each scattering indicatrix corresponds to a circular arc in Fig. 2 and the structure of this indicatrix is completely determined by the arc radius K . The indicatrix represents a set of curves displayed in polar coordinates with polar angle, which coincides with the azimuthal angle ϑ used above, and (dimensionless) radius $\omega/(vQ_0)$, where ω is the frequency loss. Each point of the indicatrix corresponds to an excitation of a QCB plasmon and therefore to a sharp peak in the scattering cross section. The number of peaks depends on the polar angle. Scanning the azimuthal angle ϑ results in changing the number of peaks. This is one

more example of dimensional crossover in QCB (see Ref.20 for similar effects in IR spectroscopy).

We start with the case of smallest radius $k \sin \varphi = -0.3Q_0$ (arc AB_1 in Fig. 2). Here all points beside the point B_1 are points of general type (i). Each one of them, e.g. point A , corresponds to excitation of two plasmons in the two arrays and therefore leads to two separate peaks in the scattering spectrum (see Fig. 4). The peaks corresponding to the point A in Fig. 2 lie at the ray defined by the angle θ_A . The point B_1 corresponds to inter-array resonance (iv) and in this direction a split doublet can be observed.

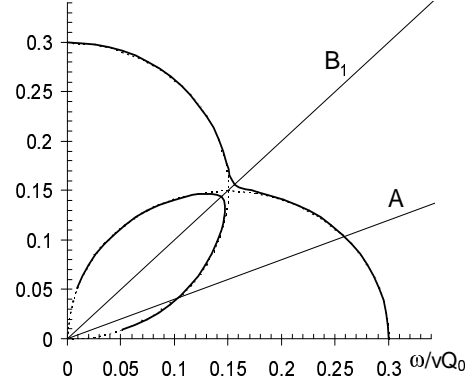


FIG. 4: Positions of the scattering peaks for $|K/Q_0| = 0.3$. The doublet in the resonance direction (point B_1 in Fig. 2) is well pronounced.

In the next case $k \sin \varphi = -0.5Q_0$ (arc $C_1B_2D_1$ in Fig. 2), as in the previous one, in general directions one can observe two single lines which form a split doublet in the resonant direction B_2 . However at the final points C_1 and D_1 the arc touches the high symmetry lines. Here the low frequency single line vanishes (there is no scattering at $Q = 0$) while the high frequency line transforms into a doublet because of an inter-band resonance (ii) in one of the arrays (Fig. 5).

Further increase of the arc radius $k \sin \varphi = -0.6Q_0$ (arc $C_2B_3D_2$ in Fig. 2) leads to appearance of two points D_2 and C_2 where the arc intersects with high symmetry lines (BZ boundaries). Each of these points generates an inter-band resonance doublet, which coexists with the low frequency single peak (Fig.6).

In the case $k \sin \varphi = -\sqrt{2}Q_0/2$ the corresponding arc includes the BZ corner B_4 . This is the point of a double inter-array and inter-band resonance (v). Moreover, here the two quartets described above coincide. Therefore, there are three lines in Fig. 7. The low-frequency line as its high-frequency partner is two-fold degenerate while the central line is four-fold degenerate. We emphasize that each quartet manifests itself in three lines, contrary to the IR absorption, where selection rules make two of them invisible.

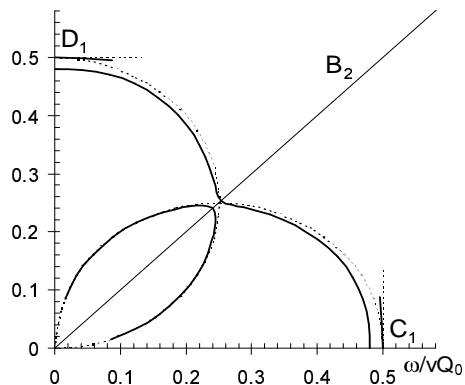


FIG. 5: Positions of the scattering peaks for $|K/Q_0| = 0.5$. Two doublets appear at the BZ boundaries (points C_1 and D_1 in Fig. 2).

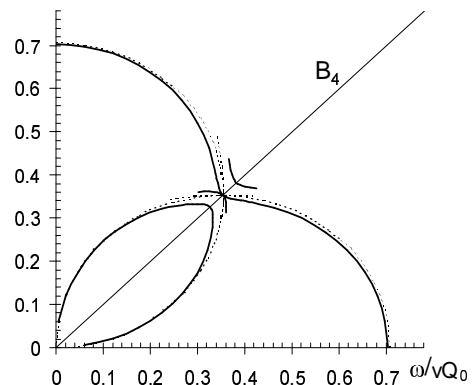


FIG. 7: Positions of the scattering peaks for $|K/Q_0| = \sqrt{2}/2$. Resonance triplet corresponding to point B_4 in Fig. 2 (two of four frequencies remain degenerate in our approximation). In IR experiments only one of the triplet components is visible.

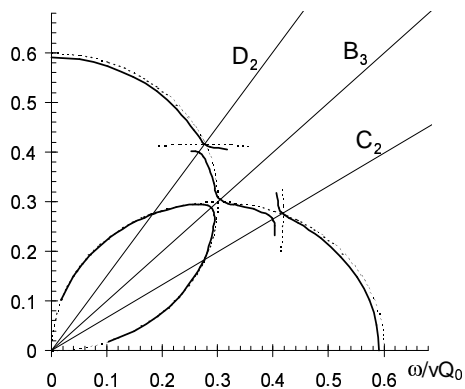


FIG. 6: Positions of the scattering peaks for $|K/Q_0| = 0.6$. Two doublets at the BZ boundaries (points C_2 and D_2 in Fig. 2) are shifted from the high symmetry directions.

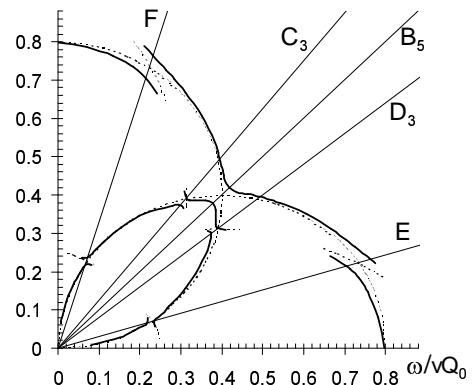


FIG. 8: Positions of the scattering peaks for $|K/Q_0| = 0.8$. Two pairs of doublets appear corresponding to excitation of two pairs of plasmons in the two arrays (points E and F in Fig. 2).

The last case $k \sin \varphi = -0.8Q_0$ demonstrates one more possibility related to inter-band resonance simultaneously in two arrays (iii). Each point E and F generates (in the corresponding direction) two doublets describing the inter-band splitting in different arrays (see Fig. 8).

IV. CONCLUSIONS

In conclusion, we studied inelastic UV Raman scattering on QCB. We derived an effective Hamiltonian for QCB-light interaction which is expressed via the same bose variables that the QCB itself. With the help of this Hamiltonian we calculated differential scattering cross section as a function of detector orientation and scattered frequency. Scanning these parameters, one can observe a set of sharp peaks in the scattering spectrum. A number of peaks and their positions strongly depend on the direction of the scattered wave vector. This results in a dimensional crossover. It manifests itself in the splitting of the peak frequencies and therefore in appearance of multiplets (mostly doublets) instead of

single lines in the scattering spectrum.

The sizes of peak splitting are determined by the nature of interaction which lifts the corresponding degeneracy. In the case of initial inter-array degeneracy, the splitting is proportional to the dimensionless interaction strength (4). The inter-band splitting is proportional to the square of this interaction. For a chosen QCB parameters it is less than the inter-array interaction strength in spite of an additional large multiplier a/r_0 . In all cases the splitting increases with increasing the interaction in QCB crosses. The peak amplitudes are proportional to the Luttinger parameter g in a single nanotube. Therefore strong electron-electron interaction suppresses the peaks.

The effectiveness of UV scattering is related to the possibility of changing continuously the excited plasmon frequency. Due to other selection rules, some lines invisible in the IR absorption spectrum, become observable in the UV scattering. UV scattering spectroscopy enables

one to restore parameters describing both interaction in QCB crosses and electron-electron interaction in a single QCB constituents.

Our studies of optical properties of QCB (this paper and Refs.20,21) show that these nanoobjects possess unique combination of optical spectra. Firstly, they are active in IR and UV frequency range. Secondly, they may be observed in various kinds of optical processes, namely direct and indirect absorption, diffraction, energy loss transmission, and Raman-like spectroscopy.

Acknowledgements

We thank Y. Imry for drawing our attention to the effectiveness of the UV scattering in probing spectral properties of QCB.

APPENDIX A: QCB PLASMONS: KINEMATICS OF INTERFERENCE.

As it was mentioned in subsection II A, standard description (5), (4), of QCB plasmons in terms of array plasmons fails at points \mathbf{Q} lying on two specific groups of lines in reciprocal space. Nevertheless, QCB plasmons even at these lines can be considered as finite combinations of array plasmons generated by the point \mathbf{Q} by more complicated way. Below we consider various types of the interference of array plasmons in QCB.

The first group of specific lines is formed by the high symmetry lines $Q_j = p_j Q_0/2$ with p_j an integer (lines parallel to coordinate axes in Fig. 2). The lines with $p_j = \pm 1$ include the BZ boundaries. In an “empty lattice” approximation, these lines are degeneracy lines which separate p_j -th and $(p_j + 1)$ -th bands of the j -th array. Inter-array interaction mixes the array states, lifts the (inter-band) degeneracy and splits corresponding frequencies. As a result, the QCB plasmons related to a point \mathbf{Q} lying on a high symmetry line (e.g. all C, D points in Fig. 2), are built from the array plasmons associated not only with the points $\mathbf{Q}_{1,2}$ but also with the symmetric (with respect to coordinate axes of a reciprocal space) points $\mathbf{Q}_{\bar{1}} = (-Q_1, q_2)$ and $\mathbf{Q}_{\bar{2}} = (q_1, -Q_2)$ (see Fig. 9).

Consider for definiteness the case $j = 1$ and assume first that the ratio $2Q_2/Q_0$ is non-integer. In this case, the point \mathbf{Q} generates three QCB plasmons. The first one of them is a $|2, Q_2\rangle$ plasmon (see Eq.5) with frequency ω_2 . The two others

$$\begin{aligned} |1, g, \mathbf{Q}_1\rangle &= \frac{1}{\sqrt{2}} (|1, \mathbf{Q}_1\rangle + |1, \mathbf{Q}_{\bar{1}}\rangle), \\ |1, u, \mathbf{Q}_1\rangle &= \frac{1}{\sqrt{2}} (|1, \mathbf{Q}_1\rangle - |1, \mathbf{Q}_{\bar{1}}\rangle) \end{aligned} \quad (\text{A1})$$

are even or odd superpositions of the 1-st array states from the two first zones with eigenfrequencies

$$\begin{aligned} \omega_{1g}(\mathbf{Q}) &= v|Q_1|, \\ \omega_{1u}(\mathbf{Q}) &= \left(1 - \frac{\phi^2 a}{r_0}\right) v|Q_1|. \end{aligned} \quad (\text{A2})$$

The case $j = 2$ is described similarly after change $1 \leftrightarrow 2$ through all this paragraph.

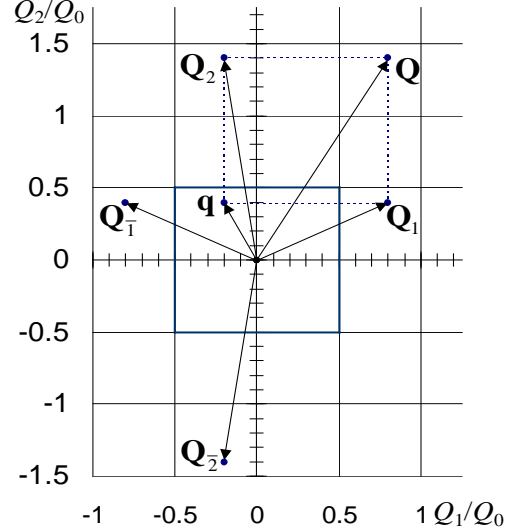


FIG. 9: QCB inverse space. The first BZ is bounded by a solid square

The second set is formed by the resonant lines defined by the equation $Q_1 + rQ_2 = nQ_0$, where $r = \pm 1$ and n are two integer parameters determining the line. In Fig. 2, resonant lines are square diagonals and lines parallel to them. In an “empty lattice” approximation, these lines are also degeneracy lines. However this degeneracy has more complicated nature. Here, array plasmons associated not only with the point \mathbf{Q} , but also array plasmons associated with the dual point $\bar{\mathbf{Q}} = (-rQ_2, -rQ_1)$ (see Fig. 10) are involved in the resonance. Inter-array interaction mixes degenerate modes, lifts the degeneracy, and splits degenerate frequencies. As a result, the QCB plasmons related to a point \mathbf{Q} at the resonant line (e.g. all B, F, E points in Fig. 2), are built from the array plasmons associated not only with the points $\mathbf{Q}_{1,2}$ but also with the symmetric (with respect to one of the bisector lines of the coordinate system of a reciprocal space) points $\bar{\mathbf{Q}}_1 = (-rQ_1, -rQ_2)$ and $\bar{\mathbf{Q}}_2 = (-rq_1, -rQ_2)$. Moreover, if the point \mathbf{Q} lies at the intersection of two resonant lines (like the point B_4 in Fig. 2), the QCB plasmons include also array states associated with the $\bar{\mathbf{Q}}_{\bar{j}}$ points.

In the general case, the point \mathbf{Q} lies only on one of the resonant lines away from the high symmetry lines. Here the point \mathbf{Q} generates two pairs of even and odd

superpositions of the first and the second array states

$$\begin{aligned} |g/u, \mathbf{Q}_1\rangle &= \frac{1}{\sqrt{2}} (|1, \mathbf{Q}_1\rangle \pm |2, \overline{\mathbf{Q}}_1\rangle), \\ |g/u, \mathbf{Q}_2\rangle &= \frac{1}{\sqrt{2}} (|2, \mathbf{Q}_2\rangle \pm |1, \overline{\mathbf{Q}}_2\rangle) \end{aligned} \quad (\text{A3})$$

whose eigenfrequencies form two doublets

$$\begin{aligned} \omega_{g/u}(\mathbf{Q}_1) &= \left(1 \pm \frac{\phi}{2}\right) v|\mathbf{Q}_1|, \\ \omega_{g/u}(\mathbf{Q}_2) &= \left(1 \pm \frac{\phi}{2}\right) v|\mathbf{Q}_2|. \end{aligned} \quad (\text{A4})$$

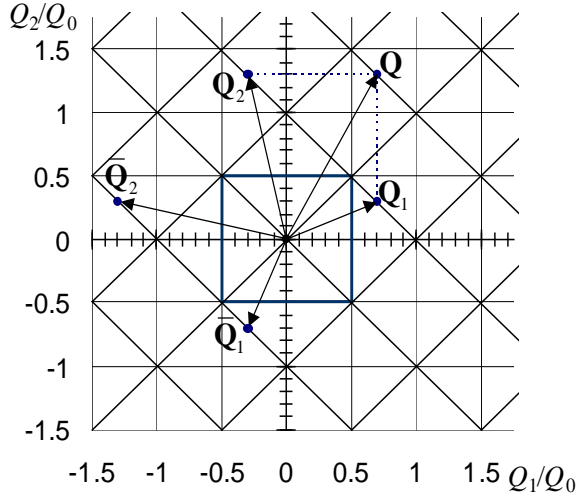


FIG. 10: Wave vectors involved in the resonance interaction. Resonant lines are displayed by solid lines.

The crossing points of resonant lines can also be divided into two groups. The first group is formed only by the crossing points of two high symmetry lines (e.g. points D_4, C_4 in Fig. 2). Here each of the generated vectors \mathbf{Q}_1 and \mathbf{Q}_2 corresponds to a pair of array eigenstates belonging to two adjacent 1D bands. Thus an *inter-band* mixing is significant in both two arrays. The corresponding QCB plasmons are even or odd combinations of j -th array plasmons ($j = 1, 2$)

$$\begin{aligned} |j, g, \mathbf{Q}_j\rangle &= \frac{1}{2} (|j, \mathbf{Q}_j\rangle + |j, \overline{\mathbf{Q}}_j\rangle), \\ |j, u, \mathbf{Q}_j\rangle &= \frac{1}{2} (|j, \mathbf{Q}_j\rangle - |j, \overline{\mathbf{Q}}_j\rangle), \end{aligned} \quad (\text{A5})$$

with eigenfrequencies

$$\begin{aligned} \omega_{j,g}(\mathbf{Q}_j) &= v \frac{Q_0 p_j}{2}, \\ \omega_{j,u}(\mathbf{Q}_j) &= \left(1 - \frac{\phi^2 a}{r_0}\right) v \frac{Q_0 p_j}{2}. \end{aligned} \quad (\text{A6})$$

The second group consists of the crosses of two resonant lines (point B_4 in Fig. 2). These point are always the crosses of two high symmetry lines. Here the QCB plasmons, generated by the point \mathbf{Q} , form two quartets. The first quartet is really generated by the point \mathbf{Q}_1 . It consists of four symmetrized combinations of single-array states

$$\begin{aligned} |g, g, \mathbf{Q}_1\rangle &= \frac{1}{2} (|1, \mathbf{Q}_1\rangle + |1, \overline{\mathbf{Q}}_1\rangle + |2, \overline{\mathbf{Q}}_1\rangle + |2, \overline{\mathbf{Q}}_1\rangle); \\ |g, u, \mathbf{Q}_1\rangle &= \frac{1}{2} (|1, \mathbf{Q}_1\rangle + |1, \overline{\mathbf{Q}}_1\rangle - |2, \overline{\mathbf{Q}}_1\rangle - |2, \overline{\mathbf{Q}}_1\rangle); \\ |u, g, \mathbf{Q}_1\rangle &= \frac{1}{2} (|1, \mathbf{Q}_1\rangle + |1, \overline{\mathbf{Q}}_1\rangle - |2, \overline{\mathbf{Q}}_1\rangle - |2, \overline{\mathbf{Q}}_1\rangle); \\ |u, u, \mathbf{Q}_1\rangle &= \frac{1}{2} (|1, \mathbf{Q}_1\rangle - |1, \overline{\mathbf{Q}}_1\rangle - |2, \overline{\mathbf{Q}}_1\rangle + |2, \overline{\mathbf{Q}}_1\rangle). \end{aligned} \quad (\text{A7})$$

QCB eigenstates of the second quartet are generated by the point \mathbf{Q}_2 . They are obtained from equations (A7) by replacing $1 \leftrightarrow 2$. Even array eigenstates are degenerate with frequencies

$$\omega_{g,g/u}(\mathbf{Q}_{1,2}) = \omega_{1,2}, \quad (\text{A8})$$

while the odd array eigenstates are split

$$\omega_{u,g/u}(\mathbf{Q}_{1,2}) = (1 \pm \phi) \omega_{1,2}. \quad (\text{A9})$$

Equations (A1) - (A9) exhaust all cases of QCB plasmons, generated by a point \mathbf{Q}_2 lying on a specific line, via the interference of array plasmons.

APPENDIX B: DERIVATION OF THE BASIC EQUATIONS OF SUBSECTION II B.

Light scattering on QCB is described by equations (7) - (13). In this Appendix we briefly explain the main steps which lead to such a description.

1. Nanotube-light interaction, Eq. (7). We start with a consideration of a single nanotube of the first array, interacting with an external electromagnetic field. The characteristic time of all nanotube energies, including Coulomb interaction, is of order of an inverse plasmon frequency. The scattering process occurs during much shorter time interval, which is of the order of an inverse photon frequency. Hence, Coulomb interaction is irrelevant for the scattering processes. This enables us to restrict ourselves to the kinetic part of the nanotube

Hamiltonian. Within the $\mathbf{k} - \mathbf{p}$ approximation, this part is given by²⁴

$$h_{kin} = v_F \int \frac{dx_1 d\gamma}{2\pi} \times \psi_\alpha^\dagger(x_1, r_0, \gamma) \hbar \mathbf{k} \cdot \boldsymbol{\sigma}_{\alpha, \alpha'} \psi_{\alpha'}(x_1, r_0, \gamma). \quad (\text{B1})$$

In the presence of a magnetic field, one should add $e\mathbf{A}/c$ to the electron momentum operator $\hbar\mathbf{k}$. An additional part of the Hamiltonian (B1) exactly coincides with the nanotube-light interaction Hamiltonian (7).

Hamiltonian (B1) is diagonalized by a two step canonical

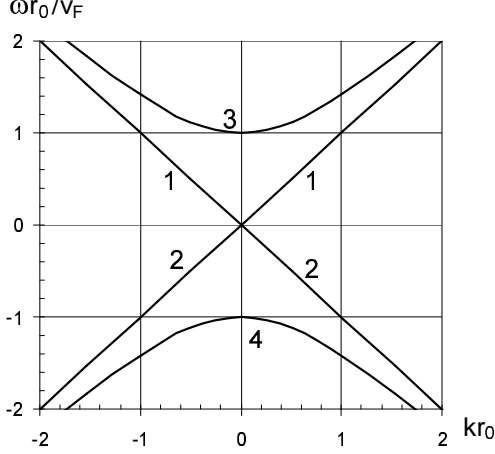


FIG. 11: The low-energy part of the band structure of a metallic nanotube. Lines 1, 3 (2, 4) correspond to excitations with $p = +1$ ($p = -1$). Lines 1, 2 (3, 4) correspond to excitations with orbital quantum number $m = 0$ ($m = \pm 1$).

transformation. The first one is Fourier transformation

$$\psi_\alpha(x_1, \gamma) = \frac{1}{\sqrt{L}} \sum_{k, m} c_{\alpha, k, m} e^{ikx_1 + im\gamma}, \quad (\text{B2})$$

where the orbital moment m is restricted by the condition $|m| \leq m_0 = [\pi r_0/a_0]$ due to the finite number of honeycomb cells along the nanotube perimeter ($a_0\sqrt{3}$ is the lattice constant). The second rotation is defined as

$$c_{p, k, m} = \frac{1}{\sqrt{2}} (c_{akm} + p e^{i\phi_m} c_{bkm}), \quad p = \pm,$$

where

$$\cos \phi_m = \frac{kr_0}{\sqrt{(kr_0)^2 + m^2}}, \quad \sin \phi_m = \frac{m}{\sqrt{(kr_0)^2 + m^2}}.$$

As a result, Hamiltonian takes the form

$$H_{kin} = \sum_{p, k, m} \hbar \omega_p(k, m) c_{pkm}^\dagger c_{pkm} \quad (\text{B3})$$

with eigenfrequencies

$$\omega_p(k, m) = p v_F \sqrt{k^2 + \frac{m^2}{r_0^2}}. \quad (\text{B4})$$

2. QCB-light interaction, Eq. (9). Substituting into Eq. (7) the scalar product $\mathbf{A} \cdot \boldsymbol{\sigma}$ in the form

$$(\mathbf{A} \cdot \boldsymbol{\sigma}) = \begin{pmatrix} 0 & A^- \\ A^+ & 0 \end{pmatrix},$$

where $A^\pm = A_1 \pm iA_\gamma$, we can write the nanotube-light interaction as

$$H_{nl} = \frac{ev_F}{c} \int \frac{dx_1 d\gamma}{2\pi} (\psi_A^\dagger A^- \psi_B + h.c.).$$

We are interested in an effective QCB-light interaction Hamiltonian obtained in second order of perturbation which describes transitions between initial states $|i\rangle$ and final ones $|f\rangle$. Initial states are one-photon states of the electromagnetic field and the electron ground state of the nanotube whereas final states consist of one photon and an electron above the Fermi level. It will be seen later that just these states form a one-plasmon array states. The energy of incident photon $E = \hbar ck$ is much larger than the excitation energies of the nanotube. Therefore, absorption of the incident photon and radiation of the scattered photon occur practically without retardation. All these result in the interaction Hamiltonian

$$h_{int} = \frac{e^2}{\hbar c} \left(\frac{v_F}{c} \right)^2 \int \frac{dx_1 d\gamma}{2\pi} \int \frac{dx'_1 d\gamma'}{2\pi} \sum_{|v\rangle} \frac{1}{k} \times \\ \left(\psi_a^\dagger(x'_1, \gamma') A^-(x'_1, 0, 0) |v\rangle \times \right. \\ \langle v | \psi_b(x'_1, \gamma') \psi_b^\dagger(x_1, \gamma) | v \rangle \times \\ \langle v | A^+(x_1, 0, 0) \psi_a(x_1, \gamma) + \\ \left. a \leftrightarrow b \right), \quad (\text{B5})$$

which corresponds to the diagram shown in Fig. 3a (there is no photons in an intermediate state).

Consider now the matrix element $\langle v | \psi_\alpha(x'_1, \gamma') \psi_\alpha^\dagger(x_1, \gamma) | v \rangle$ which enters this Hamiltonian. Due to our choice of initial and final states, only diagonal elements with respect to both virtual states $|v\rangle$ and sublattice indices α survive. In the $c_{\alpha, k, m}$ representation, (B2) they have the form

$$\langle v | \psi_\alpha(x'_1, \gamma') \psi_\alpha^\dagger(x_1, \gamma) | v \rangle = \frac{1}{L} \sum_{k, k'} \sum_{m, m'} \times \\ \langle v | c_{\alpha, k, m} c_{\alpha, k', m'}^\dagger | v \rangle e^{ikx_1 - ik'x'_1 + im\gamma - im'\gamma'}.$$

Internal matrix elements on the r.h.s. of the latter equation are

$$\langle v | c_{\alpha, k, m} c_{\alpha, k', m'}^\dagger | v \rangle = \frac{1}{2} \delta_{k, m} \delta_{k', m'}$$

(here the symmetry property $n(E_-(k, m)) + n(E_+(k, m)) = 1$ is used). Therefore

$$\langle v | \psi_\alpha(x'_1, \gamma') \psi_\alpha^\dagger(x_1, \gamma) | v \rangle = \pi \delta(x_1 - x'_1) S(\gamma - \gamma'),$$

where

$$S(\gamma) = \frac{1}{2\pi} \sum_{m=-m_0}^{m_0} e^{im\gamma}.$$

Thus, the interaction (B5) takes the form

$$h_{int} = \frac{e^2}{\hbar c} \left(\frac{v_F}{c} \right)^2 \int \frac{dx_1 d\gamma d\gamma'}{4\pi k} S(\gamma - \gamma') \times \\ A^-(x_1, 0, 0) A^+(x_1, 0, 0) \sum_{\alpha} \psi_{\alpha}^{\dagger}(x_1, \gamma') \psi_{\alpha}(x_1, \gamma).$$

The field dependent factor here is

$$A^-(x_1, 0, 0) A^+(x_1, 0, 0) = A_1^2(x_1, 0, 0) + \\ A^2(x_1, 0, 0) \sin(\gamma_A - \gamma') \sin(\gamma_A - \gamma), \quad (\text{B6})$$

and (A_1, A, γ_A) are cylindrical components of the vector potential \mathbf{A} (8). Taking into account the angular dependence of the field (B6), we can omit it in the electron operators. Indeed, according to Eq. (B4) (see also Fig. 11) in an energy-momentum region where we work, the $m = 1$ spectral band with nonzero orbital moment is separated from that with $m = 0$ by an energy of order $\hbar v_F/r_0$, which is much larger than the QCB plasmon energy. Keeping only the zero moment field operators which form the electron density operator

$$\sum_{\alpha} \psi_{\alpha}^{\dagger}(x_1) \psi_{\alpha}(x_1) = \rho(x_1) \equiv \sqrt{2} \partial_{x_1} \theta(x_1).$$

and integrating over γ, γ' , we obtain an interaction Hamiltonian in the form

$$h_{int} = \frac{\sqrt{2}}{4k} \frac{e^2}{\hbar c} \left(\frac{v_F}{c} \right)^2 \int dx_1 \partial_{x_1} \theta(x_1) \mathbf{A}_1^2(x_1, 0, 0), \quad (\text{B7})$$

where

$$\mathbf{A}_1 = \mathbf{A} + (\sqrt{2} - 1) A_1 \mathbf{e}_1.$$

Straightforward generalization of this expression to the QCB case leads exactly to the Hamiltonian (9).

3. Polarization matrix, Eq. (13). To study the scattering process, we should modify the last expression for the interaction Hamiltonian. To proceed further, we define Fourier transforms θ_{j, \mathbf{Q}_j} of the bosonic fields

$$\theta_1(x_1, n_2 a) = \frac{1}{\sqrt{NL}} \sum_{\mathbf{Q}_1} \theta_{1, -\mathbf{Q}_1} \times \\ \times e^{-iQ_1 x_1 - iQ_2 n_2 a}, \\ \theta_2(n_1 a, x_2) = \frac{1}{\sqrt{NL}} \sum_{\mathbf{Q}_2} \theta_{2, -\mathbf{Q}_2} \times \\ \times e^{-iQ_1 n_1 a - iQ_2 x_2}. \quad (\text{B8})$$

Here $N = L/a$ is the number of QCB cells in both directions. The electromagnetic field also can be expanded in

a sum of harmonics with a wave vector \mathbf{k} and polarization $\lambda = ||, \perp$,

$$\mathbf{A}(\mathbf{r}) = \sum_{\mathbf{k}\lambda} \mathbf{n}_{\mathbf{k}\lambda} A_{\mathbf{k}\lambda} e^{i\mathbf{k}\mathbf{r}}. \quad (\text{B9})$$

The polarization vectors

$$\mathbf{n}_{\mathbf{k}||} = \frac{ik_2 \mathbf{e}_1}{\sqrt{k_1^2 + k_2^2}} - \frac{ik_1 \mathbf{e}_2}{\sqrt{k_1^2 + k_2^2}}, \\ \mathbf{n}_{\mathbf{k}\perp} = \frac{k_1 k_3 \mathbf{e}_1}{k \sqrt{k_1^2 + k_2^2}} + \frac{k_2 k_3 \mathbf{e}_1}{k \sqrt{k_1^2 + k_2^2}} - \frac{\sqrt{k_1^2 + k_2^2}}{k} \mathbf{e}_3,$$

are normalized, $|\mathbf{n}_{\mathbf{k}\lambda}| = 1$, and satisfy the orthogonality conditions, $\mathbf{n}_{\mathbf{k}\lambda} \cdot \mathbf{k} = \mathbf{n}_{\mathbf{k}||} \cdot \mathbf{n}_{\mathbf{k}\perp} = 0$. The field operators $A_{\mathbf{k}\lambda}$ satisfy the condition $A_{\mathbf{k}\lambda}^{\dagger} = A_{-\mathbf{k}\lambda}$, so that $\mathbf{A}^{\dagger}(\mathbf{r}) = \mathbf{A}(\mathbf{r})$.

Substituting equations (B8), and (B9) into the Hamiltonian (9), we obtain

$$H_{int} = -i \frac{\sqrt{2NL}}{4k} \frac{e^2}{\hbar c} \left(\frac{v_F}{c} \right)^2 \sum_{\mathbf{k}, \mathbf{k}', \mathbf{Q}} \sum_{j, \lambda, \lambda'} \times \\ P_{j; \lambda', \lambda} \left(\frac{\mathbf{k}'}{k'}, \frac{\mathbf{k}}{k} \right) Q_j A_{\mathbf{k}', \lambda'}^{\dagger} A_{\mathbf{k}, \lambda} \theta_{j, -\mathbf{Q}_j}. \quad (\text{B10})$$

Here

$$P_{j; \lambda', \lambda} \left(\frac{\mathbf{k}'}{k'}, \frac{\mathbf{k}}{k} \right) = (\boldsymbol{\kappa}_{j, \mathbf{k}', \lambda'}^* \cdot \boldsymbol{\kappa}_{j, \mathbf{k}, \lambda}) \quad (\text{B11})$$

is the polarization matrix, $\mathbf{Q} = \mathbf{q} + \mathbf{m}$, and

$$\boldsymbol{\kappa}_{j, \mathbf{k}, \lambda} = \mathbf{n}_{\mathbf{k}\lambda} + (\sqrt{2} - 1) (\mathbf{n}_{\mathbf{k}\lambda} \cdot \mathbf{e}_j) \mathbf{e}_j.$$

In the case of normal incidence, Eqs. (B11), (B12) result in the form (13) of polarization matrix.

4. Scattering Hamiltonian, Eq. (12). As a next step, we express the Fourier transforms of the Bose fields θ via creation (a^{\dagger}) and annihilation (a) operators of the array plasmons

$$\theta_{j, -\mathbf{Q}_j} = \sqrt{\frac{g}{2|Q_j|}} (a_{j, -\mathbf{Q}_j} + a_{j, \mathbf{Q}_j}^{\dagger}).$$

The electromagnetic field amplitudes $A_{\mathbf{k}, \lambda}$ should also be expressed via photon creation (c^{\dagger}) and annihilation (c) operators

$$A_{\mathbf{k}, \lambda}(t) = \sqrt{\frac{\hbar c}{2V k}} (c_{\mathbf{k}, \lambda} + c_{-\mathbf{k}, \lambda}^{\dagger}).$$

Substituting these expansions into Eq. (B10) we obtain the final form of the effective interaction. *In the case of normal incidence ($\mathbf{K} = \mathbf{0}$), this interaction is written as*

$$H_{int} = \frac{i\sqrt{gNL}}{V} \left(\frac{ev_F}{2ck} \right)^2 \times \\ \sum_{\mathbf{k}, \mathbf{k}'} \sum_{j, \lambda, \lambda'} h_{\lambda', \lambda}(\mathbf{K}') c_{\mathbf{k}', \lambda'}^{\dagger} c_{\mathbf{k}, \lambda}, \quad (\text{B12})$$

where $h_{\lambda',\lambda}(\mathbf{K}')$ is the Hamiltonian (12), where $\lambda_f, \lambda_i, \mathbf{K}$ are replaced by $\lambda', \lambda, \mathbf{K}'$.

5. Scattering cross section, Eqs. (10) - (11). Standard procedure based on the Fermi golden rule leads to the following expression of the differential scattering cross section per unit QCB square

$$\frac{1}{L^2} \frac{d\sigma}{d\omega d\Omega} = \frac{1}{\pi} \left(\frac{V k_f}{L c \hbar} \right)^2 \overline{|\langle f | H_{int} | i \rangle|^2} \delta \left(\frac{\varepsilon_i - \varepsilon_f}{\hbar} \right) \quad (\text{B13})$$

(here bar denotes averaging with respect to polarization of both incident light and scattered quanta). Choose an initial ket-state $|i\rangle$ such that it contains an incident photon with momentum \mathbf{k}_i , frequency $\Omega_i = ck_i$, and polarization λ_i , and does not contain any QCB plasmon. This state can be written as $|i\rangle = |\mathbf{k}_i\rangle_l \otimes |0\rangle_p$, where $|0\rangle_p$ is the plasmon vacuum, $|\mathbf{k}_i\rangle_l = c_{\mathbf{k}_i, \lambda_i}^\dagger |0\rangle_l$, and $|0\rangle_l$ is the photon vacuum. A final bra-state $\langle f|$ contains a scattered photon with momentum \mathbf{k}_f , frequency $\Omega_f = ck_f$, and polarization λ_f . It contains also a QCB

plasmon P with the frequency ω_P (its quantum numbers will be specified below). The final state is written as $\langle f| = \langle P| \otimes \langle \mathbf{k}_f|$, where $\langle \mathbf{k}_f| = \left(c_{\mathbf{k}_f, \lambda_f}^\dagger |0\rangle_l \right)^\dagger$.

A matrix element of the interaction which enters Eq. (B13), is

$$\langle f | H_{int} | i \rangle = \langle P | \overline{H}_{int} | 0 \rangle_p, \quad (\text{B14})$$

where

$$\begin{aligned} \overline{H}_{int} &\equiv \langle \mathbf{k}_f, \lambda_f | H_{int} | \mathbf{k}_i, \lambda_i \rangle = \\ &= -\frac{i\sqrt{gNL}}{V} \left(\frac{ev_F}{2ck} \right)^2 \sum_{j, \mathbf{Q}} \frac{Q_j}{\sqrt{|Q_j|}} \delta_{\mathbf{k}_f, \mathbf{k}_i - \mathbf{Q}} \times \\ &P_{j; \lambda_f, \lambda_i} \left(\frac{\mathbf{k}_f}{k_f}, \frac{\mathbf{k}_i}{k_i} \right) \left(a_{j, -\mathbf{Q}_j} + a_{j, \mathbf{Q}_j}^\dagger \right). \end{aligned} \quad (\text{B15})$$

In the case of normal incidence Eqs. (B13) - (B15) are equivalent to Eqs. (9) - (12).

-
- ¹ J.E. Avron, A. Raveh, and B. Zur, Rev. Mod. Phys. **60**, 873 (1988).
 - ² Y. Avishai and J.M. Luck, Phys. Rev. B **45**, 1074 (1992).
 - ³ F. Guinea and G. Zimanyi, Phys. Rev. B **47**, 501 (1993).
 - ⁴ N.A. Melosh, A. Boukai, F. Dlane, B. Gerardot, A. Badolato, P.M. Petroff, and J.R. Heath, Science **300**, 112 (2003).
 - ⁵ Y. Luo, C.P. Collier, J.O. Jeppesen, K.A. Nielsen, E. De-lonno, G. Ho, J. Perkins, H-R. Tseng, T. Yamamoto, J.F. Stoddardt, and J.R. Heath, ChemPhysChem **3**, 519 (2002).
 - ⁶ T. Rueckes, K. Kim, E. Joselevich, G.Y. Tseng, C.L. Cheung, and C.M. Lieber, Science **289**, 94 (2000).
 - ⁷ R. Mukhopadhyay, C.L. Kane, and T.C. Lubensky, Phys. Rev. B **63**, 081103(R) (2001).
 - ⁸ A.B. Dalton, S. Collins, E. Muñoz, J.M. Razal, V.H. Ebron, J.P. Ferraris, J.N. Coleman, B.G. Kim, and R.H. Baughman, Nature **423**, 703 (2003).
 - ⁹ J.M. Tranquada, J. Physique IV **12**, 239 (2002).
 - ¹⁰ G.V. Tseng, J.C. Ellenbogen, Science **294**, 1293 (2001).
 - ¹¹ J.R. Heath and M.A. Ratner, Physics Today, **March**, 43 (2003).
 - ¹² M. Bockrath, D.H. Cobden, J. Lu, A.G. Rinzler, R.E. Smalley, L. Balents, and P.L. McEuen, Nature **397**, 598 (1999).
 - ¹³ R. Egger, A. Bachtold, M.S. Fuhrer, M. Bockrath, D.H. Cobden, and P.L. McEuen, in: *Interacting Electrons in Nanostructures*, p. 125, Eds. R. Haug, and H. Schoeller (Springer, Berlin, 2001).
 - ¹⁴ X.G. Wen, Phys. Rev. B **42**, 6623 (1990).
 - ¹⁵ H.J. Schultz, Int. J. Mod. Phys. **1/2**, 57 (1991).
 - ¹⁶ I. Kuzmenko, S. Gredeskul, K. Kikoin, and Y. Avishai, Low Temp. Phys. **28**, 539 (2002) [Fiz. Nizk. Temp. **28**, 752 (2002)].
 - ¹⁷ A.H. Castro Neto and F. Guinea, Phys. Rev. Lett. **80**, 4040 (1998).
 - ¹⁸ R. Mukhopadhyay, C.L. Kane, and T.C. Lubensky, Phys. Rev. B **64**, 045120 (2001).
 - ¹⁹ I. Kuzmenko, S. Gredeskul, K. Kikoin, and Y. Avishai, Phys. Rev. B **67**, 115331 (2003).
 - ²⁰ I. Kuzmenko, S. Gredeskul, K. Kikoin, and Y. Avishai, Phys. Rev. B **69**, 165402 (2004).
 - ²¹ I. Kuzmenko, Nanotechnology **15**, 441 (2004).
 - ²² S.G. Louie, in: *Carbon Nanotubes*, Eds. M.S. Dresselhaus, G. Dresselhaus, and Ph. Avouris, Topics Appl. Phys. **80**, 113 (2001), (Springer, Berlin, 2001).
 - ²³ K. Sasaki, Phys. Rev. B **65**, 195412 (2002).
 - ²⁴ H. Ajiki, T. Ando, J. Phys. Soc. Jpn. **65** 505 (1996).